

# Extraction Force and Cortical Tissue Reaction of Silicon Microelectrode Arrays Implanted in the Rat Brain

George C. McConnell, *Student Member, IEEE*, Thomas M. Schneider, D. Jason Owens, and Ravi V. Bellamkonda\*

**Abstract**—Micromotion of implanted silicon multielectrode arrays (Si MEAs) is thought to influence the inflammatory response they elicit. The degree of strain that micromotion imparts on surrounding tissue is related to the extent of mechanical integration of the implanted electrodes with the brain. In this study, we quantified the force of extraction of implanted four shank Michigan electrodes in adult rat brains and investigated potential cellular and extracellular matrix contributors to tissue-electrode adhesion using immunohistochemical markers for microglia, astrocytes and extracellular matrix deposition in the immediate vicinity of the electrodes. Our results suggest that the peak extraction force of the implanted electrodes increases significantly from the day of implantation (day 0) to the day of extraction (day 7 and day 28 postimplantation) ( $1.68 \pm 0.54$  g,  $3.99 \pm 1.31$  g, and  $4.86 \pm 1.49$  g, respectively; mean  $\pm$  SD;  $n = 4$ ). For an additional group of four shank electrode implants with a closer intershank spacing we observed a significant increase in peak extraction force on day 28 postimplantation compared to day 0 and day 7 postimplantation ( $5.56 \pm 0.76$  g,  $0.37 \pm 0.12$  g and  $1.87 \pm 0.88$  g, respectively;  $n = 4$ ). Significantly, only glial fibrillary acidic protein (GFAP) expression was correlated with peak extraction force in both electrode designs of all the markers of astroglial scar studied. For studies that try to model micromotion-induced strain, our data implies that adhesion between tissue and electrode increases after implantation and sheds light on the nature of implanted electrode-elicited brain tissue reaction.

**Index Terms**—Astroglial scar, chronic recordings, force measurement, immunohistochemistry, microelectrodes, micromotion, neuroprostheses.

Manuscript received August 2, 2006; revised January 4, 2007. This work was supported in part by the National Institutes of Health (NIH) under Grant R01 DC06849 (RVB) and Grant R01 NS 045072 (RVB), and in part by the National Science Foundation (NSF) funded Georgia Tech/Emory Center for the Engineering of Living Tissues under the Undergraduate Research Scholars (TMS) and Research Experience for Undergraduates (DJO) Programs. *Asterisk indicates corresponding author.*

G. C. McConnell and T. M. Schneider are with the Wallace H. Coulter Department of Biomedical Engineering, Georgia Institute of Technology/Emory University, Atlanta, GA 30332 USA (e-mail: georgemc@neuro.gatech.edu; thomas.schneider@bme.gatech.edu).

D. J. Owens is with the Department of Chemical Engineering and Materials Science, University of Minnesota, Minneapolis, MN 55455 USA (e-mail: owensdj@cems.umn.edu).

\*R. V. Bellamkonda is with the Wallace H. Coulter Department of Biomedical Engineering, Georgia Institute of Technology/Emory University, Atlanta, GA 30332 USA (e-mail: ravi@bme.gatech.edu).

Color versions of one or more of the figures in this paper are available online at <http://ieeexplore.ieee.org>.

Digital Object Identifier 10.1109/TBME.2007.895373

## I. INTRODUCTION

NEURAL electrode technology holds the exciting potential of allowing direct communication between nervous tissue and external electronics. This burgeoning technology has already significantly enhanced the quality of life for many patients with sensory and/or motor deficits as is evident from both the prosthetic cochlear implant, commonly used for treatment of deafness [1], [2], and deep brain stimulation, which has been used to reduce motor symptoms associated with Parkinson's Disease [3]–[5]. Silicon multielectrode arrays (Si MEAs) have been a driving force in the advancement of neural interface technology with several advantages over competitive devices including high density recording sites, batch fabrication, highly reproducible geometry, and user-customizable dimensions [6]. These micromachined neural prosthetic devices have been used to stimulate and record from the central and peripheral nervous systems [7]–[11].

However, the long-term functionality of MEAs, especially in the recording mode, is compromised by the formation of scar tissue surrounding the devices [12]–[16]. This is presumably due to implant induced astrogliosis, a process which electrically and mechanically isolates the prosthesis from the nervous system [17], [18], and causes neuronal cell loss in close proximity of the electrode surface [19], [20].

Tissue response to implants is commonly described in terms of an acute response caused by the trauma of implantation and a chronic response [17], [18]. The acute response is due to the rapid adsorption (within 1 ms) of a layer of proteins on the material upon contact with blood. This protein layer promotes attachment of platelets, neutrophils and macrophages which stimulate astrogliosis and ultimately lead to fibrous encapsulation. The chronic response is persistent due to the continued presence of the electrode: astrogliosis due to a stab wound injury is nearly absent after four weeks postinjury [20].

The response to implants in the CNS is a complex process involving interplay between at least four primary cell types: microglia/macrophages, astrocytes, meningeal fibroblasts, and neurons. Microglia are the resident macrophages of the CNS, and respond to an injury by a change in both phenotype and function, a response commonly referred to as “activation.” Pro-inflammatory cytokines released by activated microglia in turn activate astrocytes, which respond with increased expression of the intermediate filament proteins vimentin and glial fibrillary acidic protein (GFAP), along with a change in morphology [21]. The astroglial scar effectively seals off the implant, blocks

neurite growth and/or axonal regeneration, and presumably exclude neural cells by its presence immediately next to the electrode surface [22].

It has been suggested that micromotion, caused by the mechanical mismatch between Si and brain tissue, is a major factor in the chronic tissue reaction to these devices [23]. Recently, finite element modeling has been used to map the strain fields in brain tissue adjacent to Si MEAs [24], [25]. These studies concluded that the degree of electrode-tissue integration strongly influences both the distribution and magnitude of interfacial strain levels. In the bonded condition, in which tissue tightly adheres to the Si MEA, peak strain levels were lower by several orders of magnitude compared to the slip condition, in which tissue poorly adheres to the Si MEA. One study predicted regions of compression and delamination at the Si MEA tip in the case of poor adhesion between the electrode and brain tissue [25]. However, experimental data on the degree of mechanical integration of brain tissue with chronically implanted Si MEAs does not exist to inform modeling studies.

Previous studies have reported an increase in the attachment of muscle tissue to intramuscular electrodes after 7d using extraction force measurements [26], [27]. We hypothesized that with increasing implantation time, brain tissue surrounding a Si MEA would similarly anchor the MEA, even in the absence of integrative coatings. In this paper, we test this hypothesis by quantifying the force along the longitudinal axis while extracting chronically implanted Si MEAs from brain tissue <5 h (0d) postimplant (p.i.), 7d p.i., and 28d p.i. Care was taken to ensure that the measured force was from electrode-cortical tissue integration, and not from dural reestablishment around the electrode. Dura regrowth was not observed in close proximity to the bondpad for all of the implanted electrodes at the time of extraction. Peak extraction forces were then tested for correlations with state-of-the-art markers of astroglial scar at the corresponding times to investigate a potential mechanism by which the electrodes were anchored (if at all).

## II. MATERIALS AND METHODS

### A. Surgical Procedures for Chronic Implants

“Michigan probes” with four shanks were used in this study (NeuroNexus Technologies). A total of six rats, two rats per time point, were implanted with electrodes with thickness of 15  $\mu\text{m}$ , length of 4 mm, shank width of 60–100  $\mu\text{m}$ , and tip spacing of 200  $\mu\text{m}$  (abbreviated 4 mm\_200). Two electrodes were implanted in each animal at different hemispheres for a total of 12 microelectrodes used. To determine the effect of inter-shank distance on astrogliosis and peak extraction force an additional six rats, two rats per time point, were implanted with electrodes with thickness of 15  $\mu\text{m}$ , length of 3 mm, shank width of 30–100  $\mu\text{m}$ , and tip spacing of 125  $\mu\text{m}$  (abbreviated 3 mm\_125).

Adult male Sprague-Dawley rats (275–299 grams) were anesthetized for 5 min with a mixture of 5% isoflurane and 1 L/min  $\text{O}_2$  prior to surgery. Each rat was positioned into a stereotactic frame (Kopf) where anesthesia was maintained to effect ( $\sim$ 1–3% isoflurane and 0.3 L/min  $\text{O}_2$ ) during surgery by monitoring the rat’s breathing. The rat’s head was shaven over

the incision area and the skin was disinfected with isopropyl alcohol and chlorohexaderm using a slight scrubbing motion before making the incision. Ophthalmic ointment was applied to the eyes to prevent drying. A midline incision was made along the scalp, the skin retracted, and the periosteum cleared to expose the bregma. A dental drill was used to create a 3.2 mm hole at +0.2 mm anterior and +3.0 mm lateral to the bregma with a custom trephine (24 tooth  $\times$  3 mm O.D.) fabricated from stainless steel tubing (Small Parts). In order to minimize iatrogenic damage, room temperature saline was applied liberally to the spinning drill bit at the bone interface. The bone plug was carefully removed and the dura was gently pierced and retracted using a 28 gauge needle with the tip bent at a 45° angle. The bond-pad region of the microelectrode was grasped with Teflon-coated microforceps and the penetrating shanks were inserted by hand through the pia mater into the cortex. Care was taken to minimize bleeding by avoiding insertion through large surface blood vessels. The electrode was inserted to the point where only the bond-pad region was visible outside of the cortical surface. After the insertion, the bond-pad region of the electrode and the craniotomy was covered with 1% SeaKem Agarose (Cambrex) gel in phosphate buffered saline (PBS). A craniotomy of identical diameter was made over the contralateral location (+0.2 mm anterior to the Bregma and –3.0 mm lateral to the midline suture) where an additional electrode was inserted and protected with agarose the same way as described above. The craniotomies were further sealed and protected using dental acrylic anchored to the skull with bone screws (Plastics One, Inc.). The skin was closed with wound clips and the rats were monitored until recovery from anesthesia. To minimize variability associated with the surgery, all implants were performed by the same surgeon. All procedures were approved by Georgia Tech Institutional Animal Care and Use Committee.

### B. Measurement of Extraction Force

A  $\pm$ 30 g force sensor with an accuracy of 0.015 g (GSO Series Load Cell, TransducerTechniques) was mounted to a micromanipulator (Pi MP-235.5DG), which was stationed on an anti-vibration table. The micromanipulator was controlled via serial port from a computer. The output of the force sensor was low-pass filtered with a cut-off set at 150 Hz (6 dB/octave) and amplified with a gain of 2000 (Model TMO-2 Amplifier, Transducer Techniques). A 14-bit analog to digital I/O interface (USB 6009, National Instruments) was used to record the amplifier/conditioner signal output to a computer with a sampling rate of 1000 Hz. The force sensor load point was attached with a smooth banana clip; the clip was protected using Teflon tape to avoid breaking the electrode. A micrograph of the setup used to measure force while extracting the electrodes is given in Fig. 1(a).

Rats were prepared for force extraction and subsequent immunohistochemistry <5 h (0d), 7d, and 28d after device insertion. The longest time point of 28d was chosen because previous data suggests that a compact glial sheath is fully organized by this time [18]. Each rat was anesthetized with ketamine (45.65 mg/kg), xylazine (9.13 mg/kg), and acepromazine (1.52 mg/kg). Rats were then perfused intracardially

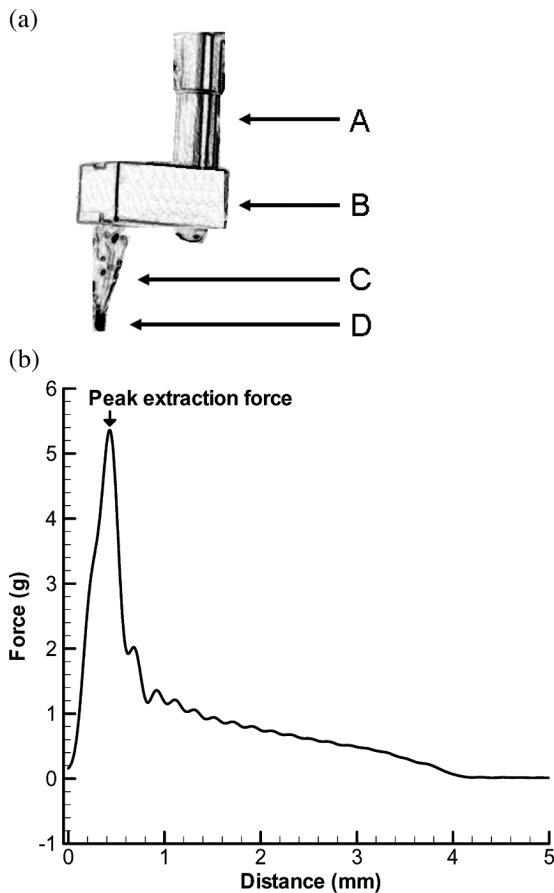


Fig. 1. (a) Schematic of the setup used to measure force while simultaneously extracting implanted probes. A computer-controlled micromanipulator (A) is mounted to a 30 g force sensor (B). A banana clip (C), coated with Teflon at the tip (D), established a connection with the exposed bond pad of the implanted electrode immediately prior to extraction of the electrode. (b) Force extraction data obtained from an electrode extracted 28d p.i. Note:  $1g = 9.807e - 3N = 980.665 \text{ dyn}$ .

with PBS prewash followed by 4% paraformaldehyde in PBS. The brains were removed by carefully cutting along the sides and anterior to the craniotomy sites and lifting off the top of the skull. Because the dura had not regrown around the implanted electrodes, when the top of the skull was lifted the electrode was not touched and remained in the brain. The brains, with electrodes in place, were postfixed for a maximum of 24 h ( $4^\circ\text{C}$ ) in 4% paraformaldehyde in PBS followed by 2 h in PBS ( $4^\circ\text{C}$ ). One brain at a time was then removed from the PBS and the bottom surface was dried and fixed to an aluminum plate using cyanoacrylate (LocTite). The glue was applied to the plate surface and the brain was held onto the aluminum surface for  $\sim 30$  s while the glue dried. The plate was then positioned under the micromanipulator-mounted force sensor.

Under visual magnification, the micromanipulator was lowered to the level of the bondpad and the clip was held open while the plate was adjusted such that the bondpad was between the teeth of the clip. The clip was then carefully closed, connecting the electrode to the force sensor. LabVIEW (National Instruments) was used to visualize and record the data collected from the force sensor. Once acquisition was started from the force sensor, the micromanipulator was raised at a constant velocity

of 1 mm/s. When it was observed that the electrode was completely removed from the brain, the micromanipulator and digital data acquisition was stopped.

### C. Analysis of Extraction Force

Postprocessing of the force measurement data consisted of low-pass filtering, baseline subtraction and identification of the maximum force using custom routines written in MATLAB. Data sets were first truncated to contain only the first 30 s of data. Including longer data sets caused errors due to inaccurate baseline calculations and/or detecting false peaks. Data were digitally filtered using a linear phase, low-pass filter (FIR1 function in MATLAB) with cutoff at 5 Hz to remove high frequency noise while the micromanipulator was moving. Data were then baseline subtracted by subtracting the mean force during the last 100 ms of the data set from the entire data set. The maximum force within each data set was identified, which we refer to as the peak extraction force. An example force-displacement recording is shown in Fig. 1(b) following digital filtering and baseline subtraction. The peak extraction force, in this case, was identified as 5.32 g.

### D. Brain Tissue Preparation for Immunohistochemistry

Following the retrieval of the electrodes, rat brains were placed into 30% sucrose ( $4^\circ\text{C}$ ) until they sunk to the bottom. A tissue dye was then carefully applied to the left-posterior hemisphere to later identify the orientation of the brain sections and align images with the same electrode orientation. The brains were then cryoprotected with Optimal Cutting Temperature (O.C.T.) compound (Tissue-Tek). Horizontal tissue sections were cut to a final depth of  $\sim 2$  mm from the surface of the cortex for all brains. Serial sections were cut  $30 \mu\text{m}$  in thickness with the exception of every 13th section, which was cut  $14 \mu\text{m}$  in thickness. The  $14 \mu\text{m}$  sections were mounted directly to glass slide and stained with Hematoxylin and Eosin (H&E) using a Leica Autostainer XL, while the  $30 \mu\text{m}$  sections were serially stored in two six-well plates at  $4^\circ\text{C}$  in PBS with 0.01% sodium azide to minimize bacterial contamination. H&E was used to visualize general tissue morphology, while immunohistochemistry was used to visualize specific cellular and extracellular matrix (ECM) markers.

### E. Immunohistochemistry of Brain Sections

To study brain tissue response, sections taken from all brains were stained simultaneously for the antibody of interest. Sections from adjacent wells, with six sections per well, were used to double-stain GFAP/vimentin, Collagen Type I (Coll I)/ED-1, and Laminin (LN)/Reca-1, respectively. These stains were used to visualize the presence of astrocytes (GFAP<sup>+</sup>, GFAP<sup>+</sup>/vimentin<sup>+</sup>), microglia (ED-1<sup>+</sup>, vimentin<sup>+</sup>), blood vessels (Reca-1<sup>+</sup>, LN<sup>+</sup>, vimentin<sup>+</sup>), fibroblasts (Coll I<sup>+</sup>, GFAP<sup>-</sup>/vimentin<sup>+</sup>), and ECM deposition of LN. The six sections per well ranged from  $\sim 200 \mu\text{m}$  to  $\sim 2$  mm below the surface of the cortex and were spaced at uniform intervals of  $374 \mu\text{m}$ . Sections were blocked in 4% normal goat serum (GIBCO) with PBS containing 0.5% Triton X-100 (Sigma) for 1 h at room temperature. Sections were then immediately incubated overnight at  $4^\circ\text{C}$  with primary antibody prepared in

TABLE I  
PRIMARY ANTIBODIES USED IN THIS STUDY

Primary	Host	Dilution	Isotype	Vendor	Specificity
GFAP	rb	1:2000	IgG	Dako	astrocytes
Vimentin	ms	1:500	IgG1	Sigma	immature and reactive astrocytes, microglia, endothelial cells and fibroblasts
Coll I	rb	1:250	IgG	Chemicon	ECM marker
CD68 (ED-1)	ms	1:1000	IgG1	Serotec	activated microglia/macrophages
LN	rb	1:500	IgG	Sigma	ECM marker
Reca-1	ms	1:500	IgG1	Serotec	endothelial cells

blocking solution. Primary antibodies used are shown in Table I. After washing in 0.5% triton in PBS, sections were incubated in secondary antibodies for 1 h at room temperature. Secondary antibodies were diluted at a ratio of 1:220 in 0.5% triton in PBS, and included goat anti-rabbit IgG(H + L) Alexa 594 (Molecular Probes) and goat anti-mouse IgG1 Alexa 488 (Molecular Probes). All sections were counterstained by incubation with the nuclear dye DAPI (Molecular Probes) that labels all cell nuclei. An additional cortical section from each rat brain was used to control for nonspecific secondary antibody labeling. Tissue sections were mounted on glass microscope slides with Fluoromount-G (Southern Biotechnology Associates).

#### F. Quantitative Analysis of Coll I/ED-1 and GFAP/Vimentin Expression

Fluorescent and brightfield images were acquired using a Microfire digital camera and a Zeiss Axioskop2 Plus upright microscope with a 10X objective, with the electrode sites centered in the camera field. Three sections approximately 200  $\mu\text{m}$ , 600  $\mu\text{m}$  and 1 mm below the brain surface were imaged for quantification due to similarities in the cortical tissue response of this region. All tissue sections were imaged in a single session to minimize variability. The exposure time was consistent within each marker and was set below saturation of the digital camera.

Fluorescent intensity as a function of distance from the electrode-tissue interface was calculated for GFAP/vimentin and Coll I/ED-1 stained sections using MATLAB (with Image Processing Toolbox, Mathworks, Natick, MA). Briefly, images were first rotated such that the four insertion sites were aligned vertically. An ellipse was computed from five or more user-specified points around each of the four insertion sites using the brightfield image to easily delineate the electrode-tissue interface and the location of the ellipses were then saved to file. Saved ellipse points were then used in the corresponding immunostained images (either GFAP/vimentin or Coll I/ED-1) to segment rectangular regions from the middle of each ellipse to a distance of 500  $\mu\text{m}$  away for both the left and right sides. The intensity values of each of the boxed regions were then averaged along the y-axis to create two mean intensity profiles for each insertion site. The mean of the eight line profiles was then computed. To correct for background differences due to nonspecific secondary antibody binding (particularly in the immediate vicinity of the insertion sites), mean profiles of identical length from primary control sections were subtracted within each group. The integral of the mean intensity profile at three different distances along the electrode

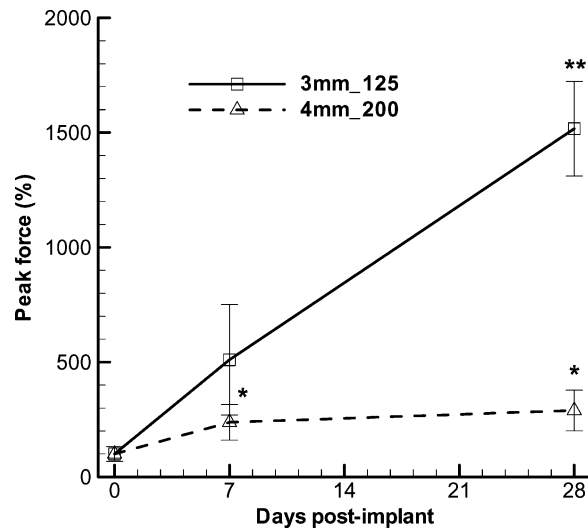


Fig. 2. The maximum force was determined from each acquired force data set (one data set from each extracted probe;  $n = 4$ ). Peak force is shown normalized to the 0d condition for two different probe designs used in this study. \*\* indicates a significant difference relative to both the 0d and 7d conditions ( $p < 0.05$ ). \* indicates a significant difference relative to the 0d condition ( $p < 0.05$ ).

(0–100  $\mu\text{m}$ , 100–300  $\mu\text{m}$ , and 300–500  $\mu\text{m}$  for GFAP/vimentin and 0–25  $\mu\text{m}$ , 25–50  $\mu\text{m}$ , and 50–100  $\mu\text{m}$  for Coll I/ED-1) was also calculated for each image.

In addition to the quantification of ED-1 intensity as a function of distance from the electrode site, ED-1 images were also quantified by estimating the number of microglia. DAPI images, which stain all cell nuclei, were used to aid in validating the presence of microglia. Images were processed with the end goal being to count only colocalized, segmented regions of ED-1 and DAPI signal indicative of microglia. ED-1 staining of microglia is highly irregular and, therefore, difficult to quantify by segmentation. DAPI staining of cell nuclei is more regular and, thus, simple, by comparison, and was segmented using a marker-based watershed algorithm. For the ED-1 images, primary controls from every condition were analyzed to estimate the common background signal. The background intensity was then subtracted from all of the ED-1 positive images. Most sections incubated with Alexa 488 secondary antibody suffered from nonspecific binding at tissue edges. In order to remove the background illumination in the immediate vicinity of the insertion site, top-hat transformation was performed. Top-hat transformation is a process which involves an estimation of background illumination followed by its subtraction from the orig-

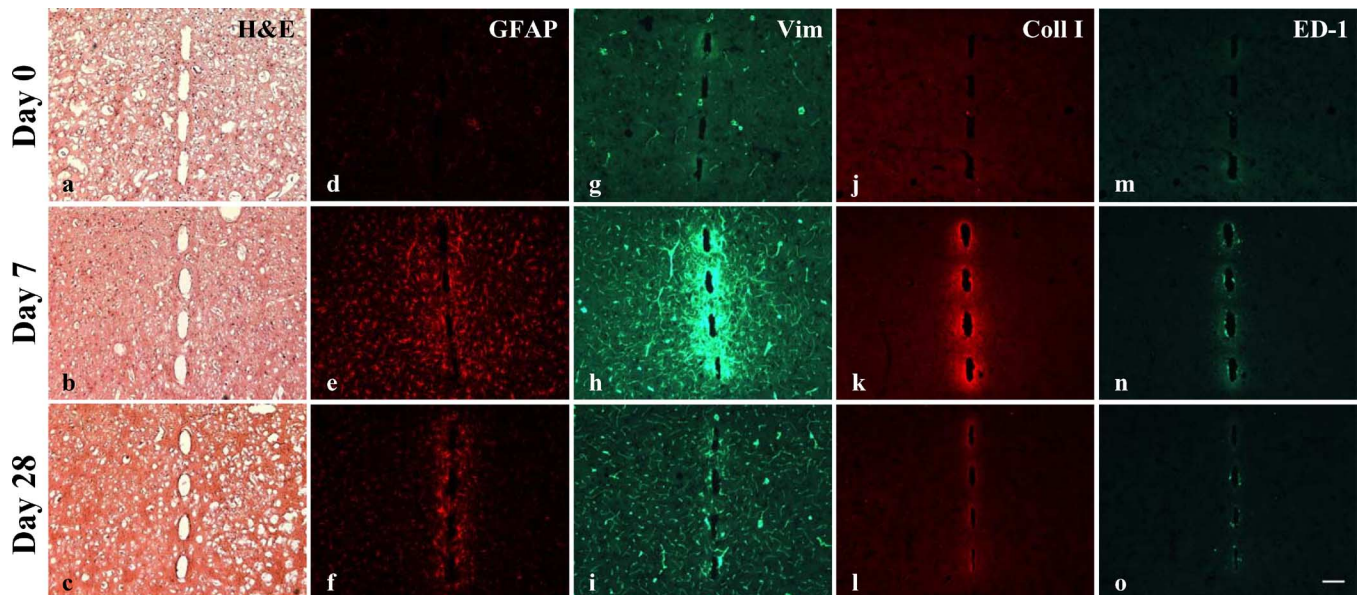


Fig. 3. (a)–(o) Representative stained sections for each of the time points studied for H&E (a)–(c), GFAP (d)–(f), vimentin (Vim) (g)–(i), collagen type I (Coll I) (j)–(l), and ED-1 (m)–(o). Sections shown are from similar depth in the cortex ( $\sim 600 \mu\text{m}$  below the brain surface). Sections were double-stained with GFAP & Vimentin or Coll I and ED-1. Regions were imaged using a 10X objective with the probe sites centered. Immunostained images were subsequently quantified. As implant duration increased, the astroglial scar became more compact (a)–(f). Vimentin, Coll I and ED-1 expression were greatest surrounding the probe sites after 7d p.i. compared to 0d and 28d p.i. (g)–(o). Scale bar =  $100 \mu\text{m}$ .

inal. The ED-1 image was then converted to a labeled image. The image of a single ED-1 label was compared with the entire segmented DAPI image. Groups of pixels with area above a pre-determined size, common in both DAPI and ED-1 images were counted as ED –  $1^+$  cells.

### G. Statistical Analysis

All statistical inferences were made between differing time points using one-way standard analysis of variance. When we found a significant difference between groups, we performed the Tukey's Honest Significant Difference (HSD) posthoc test to identify pairwise differences. Correlations were tested using Pearson's correlation coefficient and the significance was tested using Student's t-test. For all tests,  $p < 0.05$  was considered significant.

## III. RESULTS

### A. Extraction Force

We defined the peak extraction force as the maximum force within each data set acquired during electrode extraction. In both probe designs, peak extraction force increased from the day of implantation (0d p.i.) to the longest time point studied of 28d p.i. (Fig. 2). For the 4 mm<sub>200</sub> implants, baseline corrected raw peak extraction forces for 0d, 7d, and 28d p.i. were  $1.68 \pm 0.54 \text{ g}$ ,  $3.99 \pm 1.31 \text{ g}$ , and  $4.86 \pm 1.49 \text{ g}$  (mean  $\pm$  SD). The peak extraction force for both 7d p.i. and 28d p.i. was significantly higher than for 0d p.i. ( $p < 0.05$ ). No significant difference was observed between 7d p.i. and 28d p.i. forces ( $p = 0.57$ ).

For the 3 mm<sub>125</sub> implants, the baseline corrected raw peak extraction forces for 0d, 7d, and 28d p.i. were  $0.37 \pm 0.12 \text{ g}$ ,  $1.87 \pm 0.88 \text{ g}$ , and  $5.56 \pm 0.76 \text{ g}$  (mean  $\pm$  SD). The peak extraction force for 28d p.i. was significantly higher than for both

0d p.i. and 7d p.i. ( $p < 0.05$ ). A striking difference between the two designs was this significant increase in peak extraction force 28d p.i. No significant difference was observed between 0d p.i. and 7d p.i. forces ( $p = 0.058$ ).

### B. Investigating the Presence of Meningeal Fibroblasts

Coll I is a component of the ECM important to structural support. In normal healthy brain tissue, Coll I is absent, but is ubiquitous in the meninges. Coll I is, therefore, a useful marker for visualizing the presence of meningeal-derived fibroblasts in brain tissue. A thin layer, approximately  $20 \mu\text{m}$  in thickness, of intense Coll I signal was observed in 7d and 28d sections immediately adjacent to the insertion sites [Fig. 3(k) and (l)]. Coll I signal was absent in 0d sections [Fig. 3(j)].

### C. Investigating the Presence of Microglia

ED-1 is a marker specific for reactive microglia/macrophages. Immediately following implantation, no ED-1 signal was present surrounding the insertion sites [Fig. 3(m)]. After 7d ED-1 signal was present in the immediate vicinity of the insertion sites [Fig. 3(n)]. By 28d p.i., a decreased number of ED –  $1^+$  cells were observed in comparison to 7d [Fig. 3(o)]. Both 7d and 28d p.i., ED –  $1^+$  signal was primarily observed within  $50 \mu\text{m}$  of the insertion sites.

### D. Quantifying Coll I/ED-1 Expression

The intensity of Coll I and ED-1 stained sections was quantified as a function of distance from the insertion sites. Fig. 4(a) shows the distribution of Coll I surrounding the insertion site. The area under the intensity curve from 0– $25 \mu\text{m}$ , 25– $50 \mu\text{m}$ , and 50– $100 \mu\text{m}$  away from the interface are plotted as mean  $\pm$  SD [Fig. 4(c)]. Comparatively, Coll I signal 7d p.i.

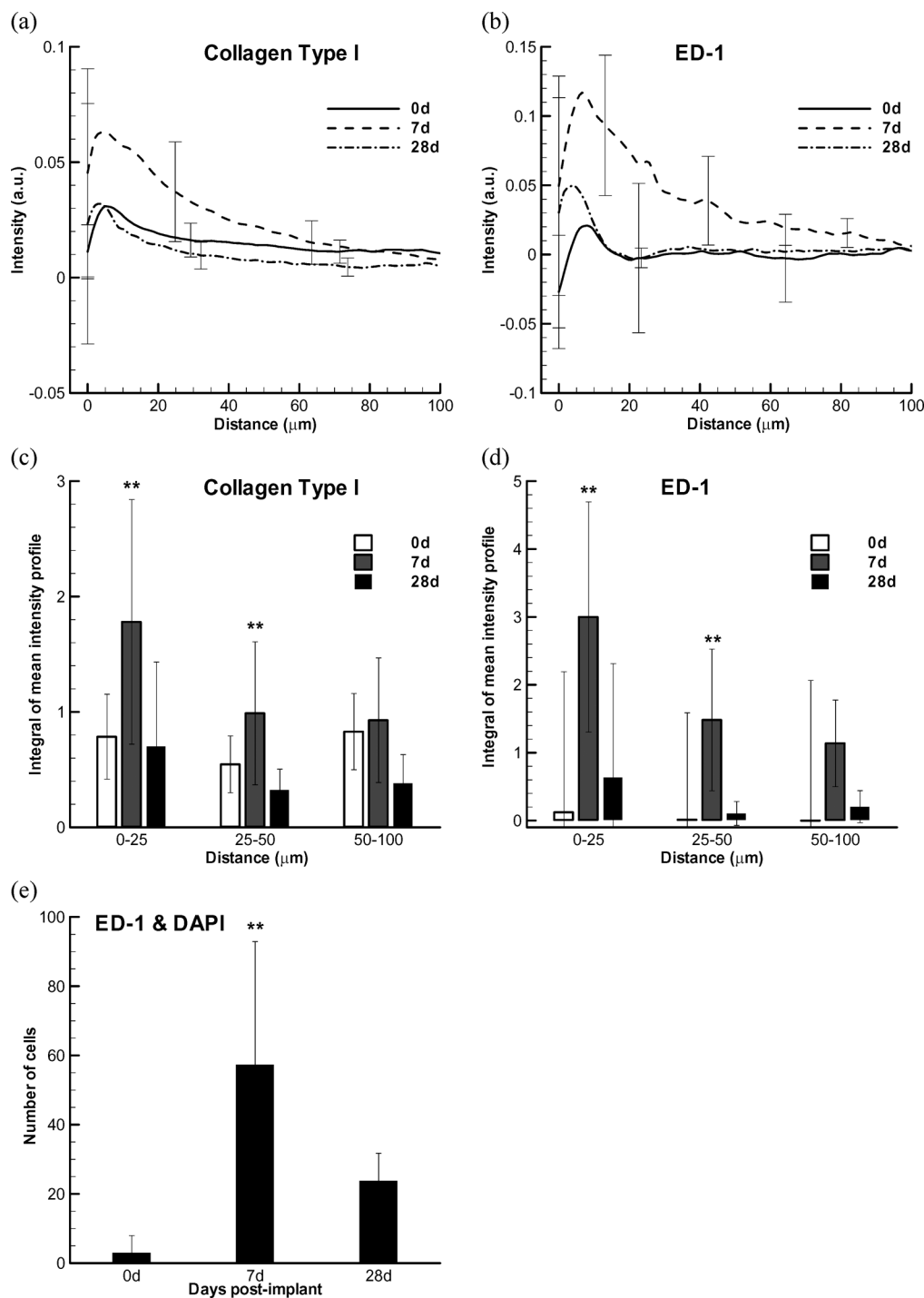


Fig. 4. (a)–(e) Coll I and ED-1 image quantification results (summary of sections  $\sim 200$ ,  $600$  and  $1000 \mu\text{m}$  below the surface of the cortex). (a) Mean  $\pm$  SD intensity profiles for Coll I. (b) Mean  $\pm$  SD intensity profiles for ED-1. The integrals from the intensity profiles were calculated  $0\text{--}25 \mu\text{m}$ ,  $25\text{--}50 \mu\text{m}$  and  $50\text{--}100 \mu\text{m}$  from the interface and used to compare intensity between groups as a function of distance from the probe site [Coll I-(c), ED-1-(d)]. \*\* indicates a significant difference relative to the 0d and 28d conditions within the same distance range ( $p < 0.05$ ). (e) Segmentation and counting of colocalized ED-1<sup>+</sup> and DAPI<sup>+</sup> regions. \*\* indicates a significant difference relative to the 0d and 28d condition within the same distance range ( $p < 0.001$  and  $p < 0.05$ , respectively).

was significantly higher than 0d and 28d p.i. within  $0\text{--}25 \mu\text{m}$  and  $25\text{--}50 \mu\text{m}$  ( $p < 0.05$ ).

Fig. 4(b) shows the distribution of ED-1 surrounding the insertion site. The area under the intensity curve from  $0\text{--}25 \mu\text{m}$ ,  $25\text{--}50 \mu\text{m}$ , and  $50\text{--}100 \mu\text{m}$  away from the interface are plotted as mean  $\pm$  SD [Fig. 4(d)]. ED-1 expression 7d p.i. was significantly higher than 0d and 28d p.i. within  $0\text{--}25 \mu\text{m}$  and

$25\text{--}50 \mu\text{m}$  ( $p < 0.05$ ). While mean intensity profiles give an indication of ED-1 signal distribution from the insertion sites, along with the general trend over time, cell counting is a common method for quantification of ED-1 signal [Fig. 4(e)]. In agreement with the intensity distribution  $0\text{--}50 \mu\text{m}$  from the insertion site, there was a significant increase in the number of microglia 7d p.i. compared to 0d and 28d p.i. ( $p < 0.05$ ).

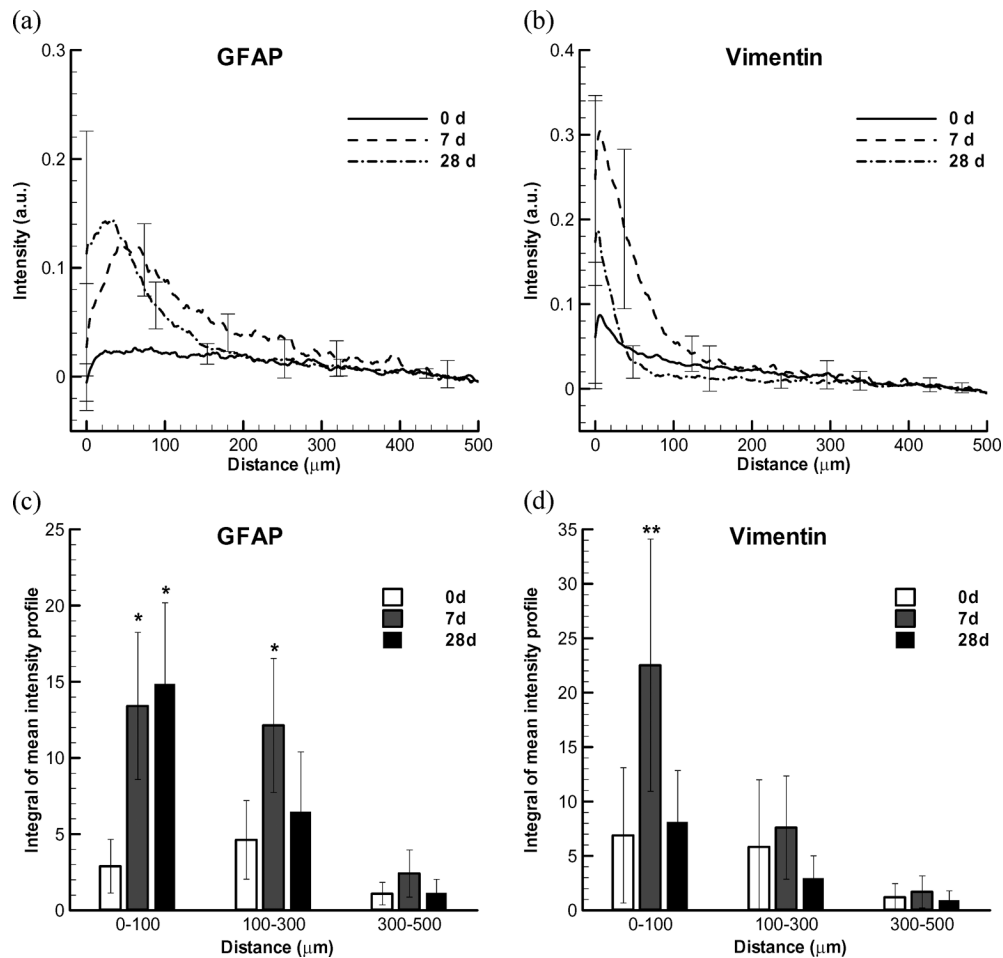


Fig. 5. (a)–(e) GFAP and vimentin image quantification results (summary of sections  $\sim 200$ ,  $600$ , and  $1000 \mu\text{m}$  below the surface of the cortex). (a) Mean  $\pm$  SD intensity profiles for GFAP. (b) Mean  $\pm$  SD intensity profiles for vimentin. The integrals from the intensity profiles were calculated  $0\text{--}100 \mu\text{m}$ ,  $100\text{--}300 \mu\text{m}$  and  $300\text{--}500 \mu\text{m}$  from the interface and used to compare intensity between groups as a function of distance from the probe site [GFAP- (c), vimentin- (d)]. \*\* indicates a significant difference relative to the 0d condition and 28d condition within the same distance range (all  $p < 0.01$ ).

### E. Investigating the Presence of Astrocytes

GFAP is a commonly used marker to visualize astrogliosis, an astrocytic reaction to injury. On the day of the implant, the insertion sites show normal resting astrocytes surrounding the implant [Fig. 3(d)]. After 7d there was a substantial increase in GFAP expression in astrocytes near the insertion sites [Fig. 3(e)]. In their reactive state, astrocytes surrounding the insertion sites became hypertrophic and elongated with thick processes. This was in contrast to astrocytes exhibiting a stellate appearance approximately  $> 300 \mu\text{m}$  away. GFAP expression was maximum immediately adjacent to the insertion site and declined progressively as a function of distance to the site. By 28d, the GFAP positive zone became compact around the insertion site, approximately  $< 100 \mu\text{m}$  in radius [Fig. 3(f)]. These astrocytes exhibited an interwoven appearance when examined at high magnification. The highly organized structure surrounding the insertion sites was similar to that observed in the H&E stained sections of the same time point [Fig. 3(c)].

### F. Investigating the Expression of Vimentin

Vimentin is expressed in immature and reactive astrocytes, microglia, fibroblasts, as well as endothelial cells. On the day

of the implant, vimentin expression was observed only in vasculature primarily  $> 100 \mu\text{m}$  from the insertion sites [Fig. 3(g)]. After 7d p.i., an amplification in vimentin expression was observed  $< 100 \mu\text{m}$  from the insertion sites [Fig. 3(h)]. After 28d p.i., vimentin expression within  $100 \mu\text{m}$  from the insertion sites had decreased compared to 7d p.i. [Fig. 3(i)].

### G. Quantifying GFAP/Vimentin Expression

The intensity of GFAP and vimentin stained sections was quantified as a function of distance from the insertion sites. Fig. 5(a) shows the distribution of GFAP surrounding the insertion site. Fig. 5(b) shows the distribution of vimentin surrounding the insertion site. The area under the intensity curve from  $0\text{--}100 \mu\text{m}$ ,  $100\text{--}300 \mu\text{m}$ , and  $300\text{--}500 \mu\text{m}$  away from the interface are plotted as mean  $\pm$  SD [Fig. 5(c)-GFAP and (d)-vimentin]. Differences in intensity were observed as a function of time. GFAP intensity was greater within  $100 \mu\text{m}$  from the insertion site after 7d p.i. and 28d p.i. compared with the 0d p.i. conditions ( $p < 0.01$ ). Vimentin intensity was greater within  $100 \mu\text{m}$  from the insertion site after 7d p.i. compared with both the 0d p.i. and 28d p.i. conditions ( $p < 0.01$ ). GFAP expression 7d p.i. was distributed over a wider region as indicated by

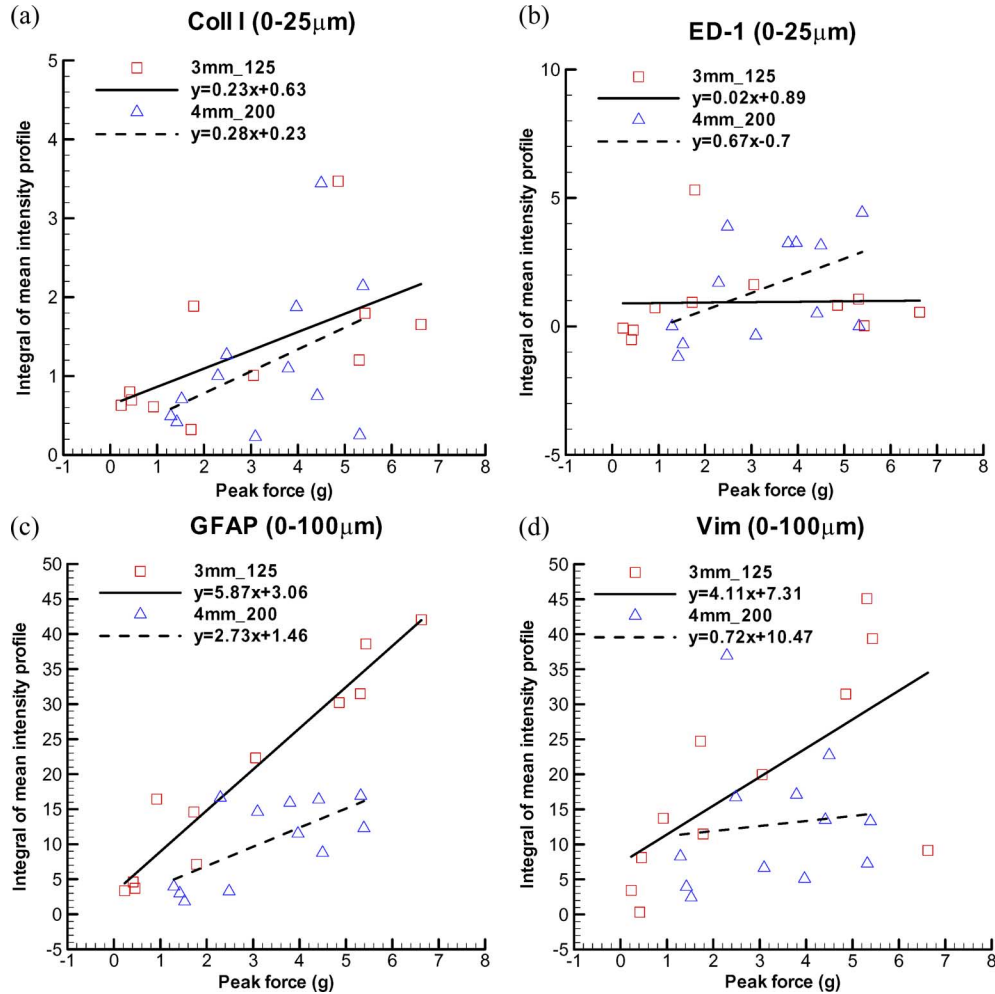


Fig. 6. (a)–(d) Scatter plots of the integrated pixel intensity for Coll I (a), ED-1 (b), GFAP (c), and vimentin (d). 0–25  $\mu\text{m}$  (a) and (b) and 0–100  $\mu\text{m}$  (c) and (d) from the interface versus peak force measured for two different probe designs. The mean pixel intensity integrals were used to give a one to one mapping between intensity and peak force. Integrated pixel intensity was chosen over the distances of (a) and (b) 0–25  $\mu\text{m}$  and (c) and (d) 0–100  $\mu\text{m}$  since the primary differences in signal intensity were within these ranges [see Figs. 4(c) and (d), and 5(c) and (d)]. Corresponding Pearson's coefficients, with p-values, are given in Table II.

significantly higher expression 100–300  $\mu\text{m}$  compared to the 0d condition ( $p < 0.01$ ).

There was a significant correlation between GFAP intensity 0–100  $\mu\text{m}$  from the insertion site and peak extraction force ( $r = 0.67$ ,  $p < 0.05$ ;  $r = 0.81$ ,  $p < 0.01$  with removal of one outlier greater than 2.5 SD from the mean) [Fig. 6(c); Table II]. No significant correlations were observed between Coll I/ED-1/vimentin and peak extraction force for the 4 mm\_200 implants [Fig. 6(a), (b), and (d), respectively; Table II]. The correlations between Coll I/vimentin and peak extraction force were still not significant after the removal of one outlier from each greater than 2.5 SD from the mean ( $r = 0.39$ ,  $p = 0.24$ ;  $r = 0.44$ ,  $p = 0.17$ , respectively).

#### H. Investigating the Influence of Intershank Distance on Astrogliosis and Peak Extraction Force

To shed further light on the relationship between intershank distance, astrogliosis, and peak extraction force, 6 additional rats were implanted with 12 electrodes and subsequently extracted at identical time points as before ( $n = 4$  per time point). It has been reported that closer shank spacing elicits a stronger

TABLE II  
RESULTS OF CORRELATION TESTING BETWEEN INTEGRATED PIXEL INTENSITY AND PEAK FORCE (DATA SHOWN IN FIG. 6)

Primary	Probe design	Pearson's coefficient (r)	p-value
Coll I	3mm_125	0.61	0.046*
Coll I	4mm_200	0.44	0.16
ED-1	3mm_125	0.024	0.94
ED-1	4mm_200	0.49	0.1
GFAP	3mm_125	0.96	1.33e-6*
GFAP	4mm_200	0.68	0.016*
Vimentin	3mm_125	0.66	0.028*
Vimentin	4mm_200	0.11	0.74

\* indicates a significant correlation between integrated pixel intensity and peak force for that particular marker ( $p < 0.05$ ). GFAP was the only marker which we studied to be significantly correlated with peak extraction force within both electrode designs.

astrocytic response [28]. We, therefore, chose an electrode design with a closer shank spacing of 125  $\mu\text{m}$  tip-to-tip. The data from one trial in the 0d group was not collected due to breakage of the electrode bondpad during insertion.

Consistent with the 4 mm\_200 design, there was a strong correlation between GFAP and peak extraction force ( $r = 0.96$ ,

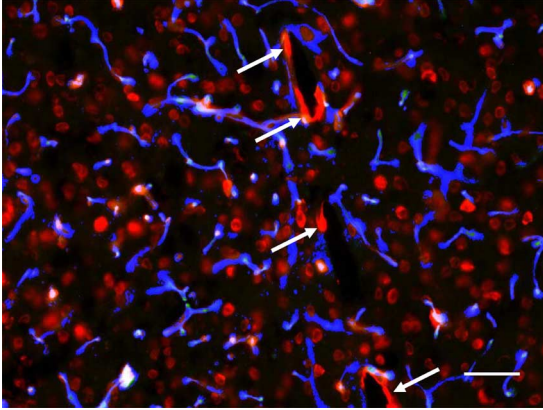


Fig. 7. Representative overlay of LN (red) and Reca-1 (green) staining from a 28d p.i. brain section, imaged using a 40X objective. The section was collected at a depth of  $\sim 600 \mu\text{m}$  below the brain surface. To aid in visualization, colocalized pixels are shown in blue. Arrows point to the strong  $\text{LN}^+/\text{Reca}^-$  signal observed at the electrode-tissue interface in the four week condition. Scale bar =  $30 \mu\text{m}$ .

$p < 0.001$ ) [Fig. 6(c)]. Also of note was that 28d p.i., both the peak extraction forces and GFAP intensity 0–100  $\mu\text{m}$  from the insertion sites were higher for the 125- $\mu\text{m}$  spaced electrodes than for the 200- $\mu\text{m}$  spaced electrodes ( $p < 0.001$ ).

Sections from the 3 mm<sub>125</sub> implanted brains were also immunostained for Coll I, ED-1, and vimentin and quantified using the same methods that were used for the 4 mm<sub>200</sub> implants. In contrast to the 4 mm<sub>200</sub> electrode design, we observed a significant correlation between Coll I and peak extraction force [Fig. 6(a); Table II] along with vimentin and peak extraction force [Fig. 6(d); Table II]. No significant correlation was observed between ED-1 and peak extraction force for the 3 mm<sub>125</sub> implants [Fig. 6(b); Table II].

#### I. Investigating Involvement of Laminin in a Mechanism for Astrocytic Adhesiveness

LN is a major component of the ECM and is found in basal lamina. It is also known that astrocytes produce LN and that the production of LN is amplified in their reactive state [29]. To study the potential influence of LN on the mechanical integration between astrocytes and the electrode, double staining of LN and Reca-1 staining was used. This method allowed detection of the presence of LN near the electrode-tissue interface, while excluding LN found in basal lamina of endothelial cells (Reca-1). We observed no LN around the interface in the 0d and 7d conditions, but sporadically observed LN at the interface for the 28d case. The intense LN signal surrounding the interface was not colocalized with Reca-1, a marker specific for endothelial cells (Fig. 7).

## IV. DISCUSSION

We observed an increase in peak extraction force while extracting electrodes as the postimplant time increased. At the onset of extraction of the electrode, the majority of the bonds between the electrode and surrounding tissue are broken which corresponds to our measurement of peak extraction force. Previous modeling results [24], [25] report that attachment of tissue to the electrodes, as we detected in our measurement of peak

extraction force, translates to a reduction in strain due to the anchoring of the electrode to the surrounding tissue. We hypothesized that over time tissue integration with the electrode would result in a higher peak extraction force, with a possible mechanism being cellular processes integrated with the surrounding ECM and the electrode. We investigated the possible cellular and matrix contributors to this increase by examining several candidate cell types including endothelial cells, microglia, astrocytes, and meningeal fibroblasts. Endothelial cells are an unlikely contributor to this increase in peak extraction force as we observed few blood vessels immediately adjacent to the insertion sites and Reca-1 signal was entirely absent from the electrodes. This observation is in contradiction to the interpretation of the  $\text{LN}^+$  signal observed on retrieved electrodes from a previously reported study, and implies that the vasculature is not in contact with the electrode surface [30]. This was also supported by stained retrieved electrodes being negative for Reca-1 (data not shown).

We examined the possibility for activated microglia being a contributor to peak extraction force increase. These cells were observed on explants 7d and 28d p.i. and immediately adjacent to the insertion sites in corresponding tissue sections. ED-1 staining showed a decreased number of microglia encircling the electrode at 28d p.i. in comparison with 7d p.i. as previously reported in rats [17], [18], [20]. However, ED-1 was uncorrelated with peak extraction force in either electrode design, suggesting that these cells are not a primary contributor to the observed force increase [Fig. 6(b); Table II].

We also examined the likelihood for meningeal cells contributing to the increase in peak extraction force. Meningeal cells are fibroblast-like cells found in the meninges, including both the dura mater and pia mater. The presence of meningeal cells at the electrode-cortical interface was evidenced by the presence of Coll I. Coll I is the most abundant form of collagen found in the body, however, it is absent in healthy neural tissue; Coll I is abundant in the pia mater [31]. The intense Coll I staining around the insertion sites near the cortical surface suggest that meningeal cells migrated, at least to some extent, along the electrode shanks into the cortical tissue. Quantitatively, however, no correlation between Coll I and peak extraction force or vimentin signal and peak extraction force was seen in the 4 mm<sub>200</sub> implants [Fig. 6(a) and (d); Table II]. This data set suggests that it is unlikely meningeal cells are a primary contributor to peak extraction force. For the 3 mm<sub>125</sub> implants a differing time course for Coll I and vimentin expression was observed. The reason for the differing response of Coll I and vimentin expression between electrode types is unclear. Due to the significant correlation between Coll I/vimentin and peak extraction force within the 3 mm<sub>125</sub> implants, a contribution from fibroblasts to the peak extraction force cannot be excluded [Fig. 6(a) and (d); Table II].

Along with previous studies investigating the electrode-tissue interface over time, we observed a compact layer of reactive astrocytes at the insertion site after 28d p.i. [17], [18]. Evidence for the contribution of astrocytes to peak extraction force is the strongest of any cell type. Qualitatively, the observed changes at the interface in astrocytes correlate temporally with peak extraction force in both electrode designs. Quantitatively, GFAP

stained sections showed the strongest positive correlations between intensity surrounding the insertion sites and peak extraction force and was the only marker which was significantly correlated with peak extraction force for both of the electrode designs [Fig. 6(c); Table II]. We further investigated LN surrounding the electrode site, as a potential mechanism by which astrocytes adhere to the electrodes. However, we observed a high variability in the presence of LN + /Reca - 1<sup>-</sup> signal near the electrode sites. This may be due to disruption of the interface during removal of the electrodes and may require a technique capable of imaging the intact electrode-tissue interface.

Our observed relationship between intershank distance, astrogliosis, and peak extraction force warrants further investigation. Significant differences were observed between the different electrode designs of 125  $\mu\text{m}$  tip spacing and 200  $\mu\text{m}$  spacing with the latter design having less astrogliosis after 28d p.i. Considering that the width of each shank for the 4 mm\_200 electrodes was approximately twice that of the 3 mm\_125 electrodes, in the case of this study, spacing of multishank MEAs had a larger influence on the chronic astrogliotic response than shank size. Shanks spaced closer together may induce more tissue reaction due to overlapping areas of tissue reaction between shanks. It may also be that the tissue within these overlapping areas responds synergistically. These observations corroborate work previously presented [28].

The electrode was not tethered to the skull in the implantation model we used. Encasing the electrode in a hydrogel, untethered, allowed us to easily remove the brain from the skull while leaving the the electrodes intact. This enabled the measurement of extraction force in the absence of complications such as presence of the dura matter, or clotted blood. However, the use of an untethered electrode model likely underestimates the tissue reaction when compared to chronic electrodes which have been tethered to the skull [20].

Due to technical challenges, we were not able to measure force contribution as a function of distance along the electrode. Therefore, we are able only to speculate on the distribution of tissue integration contributing to peak extraction force along the electrodes based on histology results from brain sections. Based on previous modeling results [24], [25], the distribution of force affects interfacial strain in two ways: in the case where 1) the force is entirely due to the pial-electrode interface with integration at the bondpad, the strain would be increased at the tip compared with the case where 2) the force is largely due to the electrode-cortical interface, with strain distributed equally along the electrode. In case 2), the strain distribution would be reduced and more uniformly distributed along the shaft compared with case 1). While case 2) is strongly supported from our results, regardless of these two distribution profiles, previous modeling results [24], [25] found that the strain fields predicted in the case where surrounding tissue is adhered to the electrode are less than the case in which the tissue is nonadherent. In other words, attachment of tissue to the electrodes translates to a reduction in strain due to the anchoring of the electrode to the surrounding tissue. The results of this study combined with previous modeling studies suggest that astrogliosis, while injurious to recording quality, may limit further injury by stabilizing chronically implanted MEAs. How effective this stabilization is

at minimizing strain is an interesting question for future studies. Currently, the precise levels of strain required to adversely affect glial cells are unknown.

## V. CONCLUSION

This paper reports the force measurement of the extraction of chronically implanted Si MEAs for three implant durations: <5 h (0d), 7d, and 28d p.i. We report that mechanical integration between tissue and implanted electrode is increased 7d and 28d p.i. compared to the day of implantation. Immunostained sections identify astrocytes as the candidate cell-type most likely to be involved in tissue-electrode adhesion.

## ACKNOWLEDGMENT

The authors would like to thank Dr. R. Lee for use of the micromanipulator and air table and R. Weinstein for instruction in operating the micromanipulator. The authors would also like to thank Dr. W. He and Dr. Y.-T. Kim for numerous helpful suggestions.

## REFERENCES

- [1] T. Bell, K. Wise, and D. Anderson, "A flexible micromachined electrode array for a cochlear prosthesis," *Sens. Actuators A*, vol. 66, pp. 63–69, 1998.
- [2] J. Rauschecker and R. Shannon, "Sending sound to the brain," *Science*, vol. 295, pp. 1025–1029, 2002.
- [3] M. Tagliati, J. Shils, C. Sun, and R. Alterman, "Deep brain stimulation for dystonia," *Expert Rev. Med. Devices*, vol. 1, pp. 33–41, 2004.
- [4] W. Liu, K. McIntire, S. Kim, J. Zhang, S. Dascalos, K. Lyons, and R. Pahwa, "Quantitative assessments of the effect of bilateral subthalamic stimulation on multiple aspects of sensorimotor function for patients with parkinson's disease," *Parkinsonism Relat. Disord.*, vol. 11, pp. 503–508, 2005.
- [5] M. Piper, G. Abrams, and W. Marks, Jr., "Deep brain stimulation for the treatment of parkinson's disease: Overview and impact on gait and mobility," *NeuroRehabilitation*, vol. 20, pp. 223–232, 2005.
- [6] J. Hetke and D. Anderson, "Silicon microelectrodes for extracellular recording," in *Handbook of Neuroprosthetic Methods*. Boca Raton, FL: CRC, 2002.
- [7] W. Rutten, H. van Wier, and J. Put, "Sensitivity and selectivity of intraneural stimulation using a silicon electrode array," *IEEE Trans. Biomed. Eng.*, vol. 38, no. 2, pp. 192–198, Feb. 1991.
- [8] A. Branner, R. Stein, and R. Normann, "Selective stimulation of cat sciatic nerve using an array of varying-length microelectrodes," *J. Neurophysiol.*, vol. 85, pp. 1585–1594, 2001.
- [9] D. Kipke, R. Vetter, J. Williams, and J. Hetke, "Silicon-substrate intracortical microelectrode arrays for long-term recording of neuronal spike activity in cerebral cortex," *IEEE Trans. Neural Syst. Rehabil. Eng.*, vol. 11, no. 2, pp. 151–155, Jun. 2003.
- [10] R. Vetter, J. Williams, J. Hetke, E. Nunamaker, and D. Kipke, "Chronic neural recording using silicon-substrate microelectrode arrays implanted in cerebral cortex," *IEEE Trans. Biomed. Eng.*, vol. 51, no. 6, pp. 896–904, Jun. 2004.
- [11] L. Hochberg, M. Serruya, G. Friehs, J. Mukand, M. Saleh, A. Caplan, A. Branner, D. Chen, R. Penn, and J. Donoghue, "Neuronal ensemble control of prosthetic devices by a human with tetraplegia," *Nature*, vol. 442, no. 7099, pp. 164–171, 2006.
- [12] P. Rousche and R. Normann, "Chronic recording capability of the Utah intracortical electrode array in cat sensory cortex," *J. Neurosci. Meth.*, vol. 82, p. 115, 1998.
- [13] J. Williams, R. Rennaker, and D. Kipke, "Long-term neural recording characteristics of wire microelectrode arrays implanted in cerebral cortex," *Brain Res. Protoc.*, vol. 4, pp. 303–313, 1999.
- [14] X. Liu, D. B. McCreery, R. R. Carter, L. A. Bullara, T. G. H. Yuen, and W. F. Agnew, "Stability of the interface between neural tissue and chronically implanted intracortical microelectrodes," *IEEE Trans. Rehabil. Eng.*, vol. 7, no. 3, pp. 315–326, Sep. 1999.
- [15] M. A. L. Nicolelis, D. Dimitrov, J. M. Carmena, R. Crist, G. Lehew, J. D. Kralik, and S. P. Wise, "Chronic, multisite, multielectrode recordings in macaque monkeys," *PNAS*, vol. 100, pp. 11 041–11 046, 2003.

- [16] G. Santhanam, S. Ryu, B. Yu, A. Afshar, and K. Shenoy, "A high-performance brain-computer interface," *Nature*, vol. 442, no. 7099, pp. 195–198, 2006.
- [17] J. Turner, W. Shain, D. Szarowski, M. Andersen, S. Martins, M. Isaacson, and H. Craighead, "Cerebral astrocyte response to micromachined silicon implants," *Exp. Neurol.*, vol. 156, pp. 33–49, 1999.
- [18] D. Szarowski, M. Andersen, S. Rettererc, A. Spencec, M. Isaacsonc, H. Craighead, J. Turner, and W. Shain, "Brain responses to micromachined silicon devices," *Brain Res.*, vol. 983, pp. 23–35, 2003.
- [19] D. Edell, V. Toi, V. McNeil, and L. Clark, "Factors influencing the biocompatibility of insertable silicon microshafts in cerebral cortex," *IEEE Trans. Biomed. Eng.*, vol. 39, no. 6, pp. 635–643, Jun. 1992.
- [20] R. Biran, D. Martin, and P. Tresco, "Neuronal cell loss accompanies the brain tissue response to chronically implanted silicon microelectrode arrays," *Exp. Neurol.*, vol. 195, pp. 115–126, 2005.
- [21] J. Fawcett and R. Asher, "The glial scar and central nervous system," *Brain Res. Bull.*, vol. 49, pp. 377–391, 1999.
- [22] J. Silver and J. Miller, "Regeneration beyond the glial scar," *Nat. Rev. Neurosci.*, vol. 5, pp. 146–156, 2004.
- [23] V. Polikova, P. Tresco, and W. Reichert, "Response of brain tissue to chronically implanted neural electrodes," *J. Neurosci. Meth.*, vol. 148, no. 1, pp. 1–18, 2005.
- [24] H. Lee, R. Bellamkonda, W. Sun, and M. Levenston, "Biomechanical analysis of silicon microelectrode-induced strain in the brain," *J. Neural Eng.*, vol. 2, pp. 81–89, 2005.
- [25] J. Subbaroyan, D. Martin, and D. Kipke, "A finite-element model of the mechanical effects of implantable microelectrodes in the cerebral cortex," *J. Neural Eng.*, vol. 2, pp. 103–113, 2005.
- [26] N. Bhadra and J. Mortimer, "Extraction forces and tissue changes during explant of cwru-type intramuscular electrodes from rat gastrocnemius," *Ann. Biomed. Eng.*, vol. 25, no. 6, pp. 1017–1025, 1997.
- [27] N. Bhadra and J. Mortimer, "Extraction force and tissue change during removal of a tined intramuscular electrode from rat gastrocnemius," *Ann. Biomed. Eng.*, vol. 34, no. 6, pp. 1042–1050, 2006.
- [28] S. Oh, K. Smith, C. Bjornsson, J. Turner, J. Song, S. Kim, and W. Shain, "Regional differences of reactive responses against silicon neural probe implanted into deep brain regions," presented at the Neural Prosthesis Workshop, Bethesda, MD, Oct. 2003.
- [29] P. Liesi, S. Kaakkola, D. Dahl, and A. Vaheri, "Laminin is induced in astrocytes of adult brain by injury," *EMBO J.*, vol. 3, no. 3, pp. 683–686, 1984.
- [30] L. Spataro, J. Dilgen, S. Retterer, A. Spence, M. Isaacson, J. Turner, and W. Shain, "Dexamethasone treatment reduces astroglia responses to inserted neuroprosthetic devices in rat neocortex," *Exp. Neurol.*, vol. 194, pp. 289–300, 2005.
- [31] G. Shellswell, D. Restall, V. Duance, and A. Bailey, "Identification and differential distribution of collagen types in the central and peripheral nervous systems," *FEBS Lett.*, vol. 106, no. 2, pp. 305–308, 1979.



**George C. McConnell** (S'01) received the B.S. and M.S. degrees in biomedical engineering from Drexel University, Philadelphia, PA, in 2003. He is currently working toward the Ph.D. degree at the Georgia Institute of Technology, Atlanta.

His research interests lie in neural prostheses, tissue engineering, biomaterials, electrophysiology, and image processing. His current work is focused on developing techniques to monitor and modulate scar tissue surrounding cortical microelectrode arrays.

Dr. McConnell is a Student Member of the IEEE Engineering in Medicine and Biology Society.



**Thomas M. Schneider** received a B.S. degree in biomedical engineering from the Georgia Institute of Technology, Atlanta, in 2006. He is currently an intern at Philips Medical Systems in Cleveland, Ohio, and is hoping to pursue a career in medicine in the near future.

His research interests include neural prostheses, the quantitative analysis of immunohistological images, as well as novel 3-D reconstruction and image processing techniques.



**D. Jason Owens** received B.S. degrees in chemical engineering and mathematics from the University of South Carolina, Columbia, in 2005. He is currently working toward the Ph.D. degree in chemical engineering at the University of Minnesota, Twin Cities.

His research interests include the investigation of the regulation of proliferation, differentiation, and lineage commitment of normal stem cells.



**Ravi V. Bellamkonda** received the B.S. degree in biomedical engineering from Osmania University, India, in 1989 and the Ph.D. degree in medical sciences from Brown University (with P. Aebischer), Providence, RI, in 1994.

From 1994 to 1995, he was a Markey Postdoctoral Fellow in the Department of Brain and Cognitive Sciences at Massachusetts Institute of Technology, Cambridge. In 1995, he was appointed to the Biomedical Engineering faculty at Case Western Reserve University, Cleveland, OH. In 2003, he joined the faculty

of the Wallace H. Coulter Department of Biomedical Engineering at Georgia Tech/Emory, Atlanta, GA. He is currently Professor with tenure, directs the Neurological Biomaterials and Therapeutics group, and leads the Neural Tissue Engineering Thrust in an NSF funded ERC "Georgia Tech/Emory Center for Engineering Living Tissues." His primary research interests include developing anisotropic scaffolds for peripheral nerve regeneration, understanding and overcoming glial scar mediated regenerative failure in the CNS, developing nano-scale drug and contrast agent delivery vehicles for brain tumors, and interfacing technologies that will better integrate external electronics to the nervous system.